Received: 18 July 2022 | Revised: 5 January 2023 | Accepted: 13 March 2023

DOI: 10.1049/itr2.12356

IET Intelligent Transport Systems

The Institution of Engineering and Technology WILEY

ORIGINAL RESEARCH

Impact of the tyre dynamics on autonomous vehicle path following control with front wheel steering and differential motor torque

Shilei Zhou[1,2] | Yang Tian[1] | Paul Walker[2] | Nong Zhang[2]

[1]School of Mechanical Engineering, Yanshan University, Qinhuangdao, China

[2]Faculty of Engineering and Information Technology, University of Technology Sydney, Sydney, Australia

Correspondence
Yang Tian, No. 438 West Hebei Avenue, Qinhuangdao 066004, Hebei Province, P.R. China.
Email: yang.tian@ysu.edu.cn

Funding information
Natural Science Foundation of Hebei Province, Grant/Award Number: E2021203085; Yanshan University, Grant/Award Number: 2021LGQN008; Hebei Province Department of Education, Grant/Award Number: C20220330

Abstract

This paper investigates the impact of tyre dynamics on autonomous vehicle dynamic control. The commonly used 2 degrees of freedom bicycle model and a detailed vehicle model considering tyre dynamics are built, respectively, to describe the vehicle dynamics. The two models are firstly compared with the response to front wheel steering input and differential motor torque input. The transient vehicle body vibrations are clearly demonstrated by the detailed model but overlooked by the bicycle model. The influence of tyre nonlinearity on path offset is also revealed. Then, the path following control strategy is designed based on the linear quadratic regulator control to compare the two models from the path following performance perspective. The double lane change simulation is conducted. The results show that at low vehicle speed, the path following errors of two models are very close, which proves the rationality of using the bicycle model to represent the vehicle dynamics in mild and moderate driving conditions. However, when the path following is conducted with high vehicle speed, the required lateral tyre force is large, so the tyres work with large slip angles and the tyre nonlinearity generates significant deviation on the path following errors between the two models.

1 | INTRODUCTION

Intelligent transportation is widely accepted as the trend of future transportation where the autonomous vehicle is one of the most important elements [1]. In the autonomous vehicle, the vehicle driving control such as steering, accelerating and braking are realized by automatic actuators rather than the driver. At the same time, the in-wheel drive electric vehicle is also attracting more and more attention owing to its advantages of electric driving and independent motor torque output in each wheel [2]. With rapid torque response of the in-wheel motor, direct yaw moment (DYM) control is achievable for vehicle dynamic control, especially for vehicle stability and path following control [3, 4].

In the autonomous vehicle with in-wheel drive and front wheel steering (FWS), the FWS and DYM are individually or jointly used for vehicle dynamic control such as collision avoidance control [5], rollover prevention control [6] and path following control [7]. In reference [8], a model predictive control (MPC) based controller which integrates FWS control and DYM control is designed to improve vehicle stability. In reference [9], the required lateral force and yaw moment to maintain vehicle stability are calculated by nonlinear MPC and then transformed to FWS input and differential motor torque (DMT) input through particle swarm optimization. In reference [10], a fuzzy proportional-integral-derivative (PID) based FWS control strategy is designed to improve the steering system response speed and control accuracy with increased steering system inertia and resistance caused by in-wheel motor. In reference [11], slide mode control (SMC) is proposed to track the vehicle sideslip angle and yaw rate with external disturbance and parameter uncertainties. In reference [12], a vehicle stability index is designed according to the front and rear tire slip angles. Then a SMC controller is designed to control motor torque with the sliding surface weight adjusted by the stability index. In reference [13], network-induced time varying delay is considered when designing vehicle lateral motion control strategy in which H_∞-based linear quadratic regulator (LQR) controller is adopted to deal with the time delay problem.

The path following control is a combination of longitudinal speed following and lateral dynamic control. PID control and preview control are adopted in reference [14] to design an autonomous vehicle speed following control strategy which is tested on a MKZ platform. In reference [15], the coordinated longitudinal and lateral control of an autonomous vehicle is realized by an output-feedback triple-step controller. The path following performance is verified by typical manoeuvres such as double-lane change. Reference [16] designs a composite nonlinear feedback path following control strategy considering the tyre force saturation. This control strategy helps eliminate the steady-state error and improve transient performance. In reference [17], a path following control strategy is proposed based on immersion and invariance control theory. It is proved to be effective under variable driving conditions, disturbance and parameter uncertainties.

As shown in above references, most of the vehicle stability and path following control research is based on simplified vehicle models where the 2 degrees of freedom (DOF) bicycle model is the most popular one. In the bicycle model, the tyre carcass dynamics are overlooked for the sake of controller design. The tyre road force generated by FWS and DMT is treated to act on vehicle body directly to control the vehicle yaw rate and sideslip [15, 18]. At the same time, research on tyre dynamics proves that tyre has nonlinearity, hysteresis and vibration which significantly affect vehicle dynamics and shouldn't be overlooked. The rigid ring tyre model [19, 20] proposed and verified by Hans B. Pacejka comprehensively describes the tyre vibration characterises. The tire response to braking torque is researched in reference [21] which indicates the potential impact of tyre dynamics on vehicle longitudinal dynamics. The tested tyre dynamic response is great close to the theoretical models, which verifies the tyre model. To describe the tyre force hysteresis, relaxation length [22] is introduced which makes tyre force equation nonlinear. These nonlinear models can well describe the tyre carcass dynamics however are hard to be implemented to design advanced vehicle dynamic control strategies which are based on the state space method [23, 24].

In addition to vehicle dynamics control, different vehicle models with different complexity are also adopted for other specific research targets, such as vehicle pose estimation [25, 26] and vehicle sideslip angle estimation [27]. Although model simplification is beneficial for controller design, it potentially makes the vehicle model deviate from the real vehicle dynamics when large and rapid control inputs are required for vehicle dynamic control during emergency conditions such as collision avoidance [28]. Furthermore, in the autonomous vehicles with in-wheel drive, the unsprung mass, steering system inertia and wheel rotational inertia are significantly increased, which makes the tyre dynamics such as transient vibration and hysteresis have more impact on vehicle dynamics [29, 30].

As found from the references, research on vehicle dynamics and control are quite separate. On one hand, the control-oriented research normally simplifies the vehicle dynamics or even totally overlooks the tyre dynamics, such as the bicycle model. On the other hand, the research on tyre dynamics demonstrates the tyre has significant nonlinearity, hysteresis and transient vibration. It seems the simplified vehicle models have been "overused" in vehicle dynamic control research, especially in research where the nonlinearity and transient vibration should be considered, such as emergent collision avoidance and tyre saturated scenarios.

To this end, in this paper, the impact of tyre dynamics on autonomous vehicle path following control is researched. Firstly, the bicycle model and a detailed vehicle model with tyre dynamics are built. The vehicle transient and steady-state response to FWS and DMT input are researched. Then the path following control strategy is designed based on LQR control and the double lane change is conducted to compare the two models' path following performance. The results reveal the remarkable impact of tyre dynamics on both transient and steady-state vehicle dynamics. From this research, it is demonstrated that for mild and moderate driving and lateral dynamic control which use a small or middle amount of tyre-road force, it is suitable to use the simplified vehicle model to represent the vehicle dynamics. However, it should be noticed that for the vehicle dynamic control under a large lateral force such as during emergency collision avoidance or under tyre saturation scenarios, special attention should be paid to make sure the transient vehicle dynamic movements are still within the safety criteria.

The remainder of this paper is organized as follows: In Section 2, the bicycle model is built to analyse the vehicle dynamics. Section 3 conducts vehicle dynamic analysis considering the tyre dynamics. In Section 4, vehicle dynamic response to FWS and DMT inputs is researched and compared between two models. Section 5 designs the path following control strategy based on LQR control. In Section 6, double lane change is conducted to compare the bicycle model and detailed model path following performance. Conclusion is drawn for this paper in Section 7.

2 | VEHICLE DYNAMIC ANALYSIS WITH BICYCLE MODEL

The 2 DOF bicycle model is shown in Figure 1 [11, 31]. In the bicycle model, vehicle is treated as symmetrical to its longitudinal axis. The suspension dynamics and tyre carcass dynamics are overlooked, which means the tyre road contact force is transferred to vehicle body directly.

Based on the small FWS angle assumption [32], the vehicle longitudinal, lateral and yaw dynamics are described by Equations (1)–(3):

$$m_g\dot{v}_x = F_{xf} + F_{xr} + m_g\dot{\gamma}v_y, \tag{1}$$

$$m_g\dot{v}_y = F_{yf} + F_{yr} - m_g\dot{\gamma}v_x, \tag{2}$$

$$I_{zg}\ddot{\gamma} = F_{yf}l_f - F_{yr}l_r + M_\gamma, \tag{3}$$

where m_g is the total vehicle mass, I_{zg} is the vehicle yaw inertia, v_x and v_y are vehicle longitudinal and lateral speeds, γ is vehicle

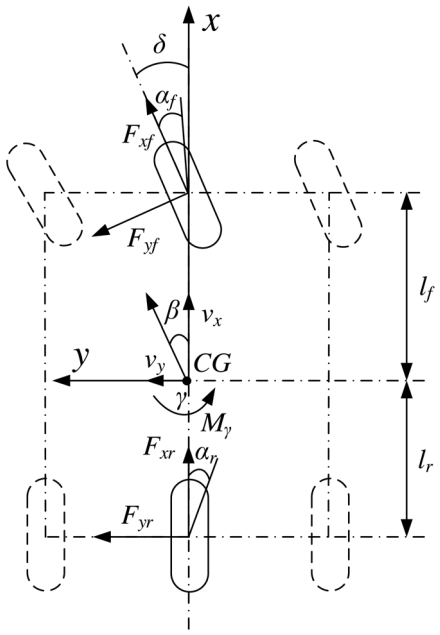

FIGURE 1 2 DOF bicycle model.

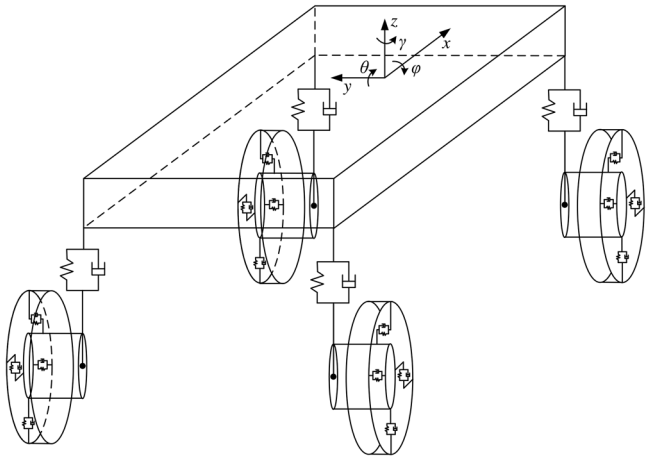

FIGURE 2 Detailed vehicle model considering tyre dynamics.

yaw angle, F_{xf} and F_{xr} are longitudinal force of front and rear tyres, F_{yf} and F_{yr} are lateral force of front and rear tyres, M_γ is DYM, l_f and l_r are the front and rear wheelbases.

In the bicycle model, the lateral force is obtained from the constant tyre cornering stiffness and slip angle, as shown in Equation (4):

$$F_{yf} = -2c_f\alpha_f, F_{yr} = -2c_r\alpha_r, \tag{4}$$

where c_f and c_r are the cornering stiffness of front and rear tyres, α_f and α_r are slip angles of front and rear tyres, which are obtained by vehicle movement and FWS angle according to Equation (5):

$$\alpha_f = \beta - \delta + \frac{l_f\dot{\gamma}}{v_x}, \alpha_r = \beta - \frac{l_r\dot{\gamma}}{v_x}, \tag{5}$$

where δ is FWS angle, β is vehicle sideslip angle which can be defined as v_y/v_x with small angle assumption [33].

Because the tyre dynamics are overlooked, the motor torque at each wheel is directly transformed into vehicle longitudinal driving force [3, 34], as shown in the following equation:

$$F_x = \frac{T_m - I_w\dot{\omega}_w}{r_e}, \tag{6}$$

where T_m is motor torque, I_w is the wheel rotational inertia, ω_w is wheel rotational speed, r_e is the tyre effective radius.

3 | VEHICLE DYNAMIC ANALYSIS WITH A DETAILED MODEL CONSIDERING TYRE DYNAMICS

To investigate the effect of tyre dynamics on vehicle path following control with FWS and DMT, a more detailed vehicle model is built considering the tyre dynamics, as shown in Figure 2. In this detailed model, the vehicle suspension dynamics are also included to reflect the tyre vertical load variations caused by vehicle body movements during accelerating, braking and steering.

3.1 | Vehicle body dynamic analysis

In the detailed model, the tyre-road force is transmitted to vehicle body through the tyre carcass, motor body, strut assembly and suspension. Vehicle body could move vertically with respect to the motors owing to the suspension elasticity. However, lateral and longitudinal motions between vehicle body and motors are restricted by the strut assembly. So, it is considered that the vertical force acting on vehicle body is from the suspension while the lateral and longitudinal forces are from the strut assembly. Therefore, vehicle body vertical, roll and pitch motions are modelled by Equations (7)–(9). In the modelling, roll and pitch motions are treated as decoupled [3, 35, 36].

$$m_v\ddot{z} = F_{zfl} + F_{zfr} + F_{zrl} + F_{zrr} \tag{7}$$

$$I_x\ddot{\varphi} = l_t(F_{zfl} + F_{zrl} - F_{zfr} - F_{zrr}) + m_v h_r(\dot{v}_y + \dot{\gamma}v_x), \tag{8}$$

$$I_y\ddot{\theta} = l_r(F_{zrl} + F_{zrr}) - l_f(F_{zfl} + F_{zfr}) - m_v h_p(\dot{v}_x - \dot{\gamma}v_y), \tag{9}$$

$$\begin{cases} F_{zfl} = k_{sf}(z_{mfl} - z_{fl}) + c_{sf}(\dot{z}_{mfl} - \dot{z}_{fl}) \\ F_{zfr} = k_{sf}(z_{mfr} - z_{fr}) + c_{sf}(\dot{z}_{mfr} - \dot{z}_{fr}) \\ F_{zrl} = k_{sr}(z_{mrl} - z_{rl}) + c_{sr}(\dot{z}_{mrl} - \dot{z}_{rl}) \\ F_{zrr} = k_{sr}(z_{mrr} - z_{rr}) + c_{sr}(\dot{z}_{mrr} - \dot{z}_{rr}) \end{cases}, \tag{10}$$

where m_v is the vehicle body mass, I_x and I_y are the vehicle body roll and pitch inertias, z, φ and θ are vehicle body vertical,

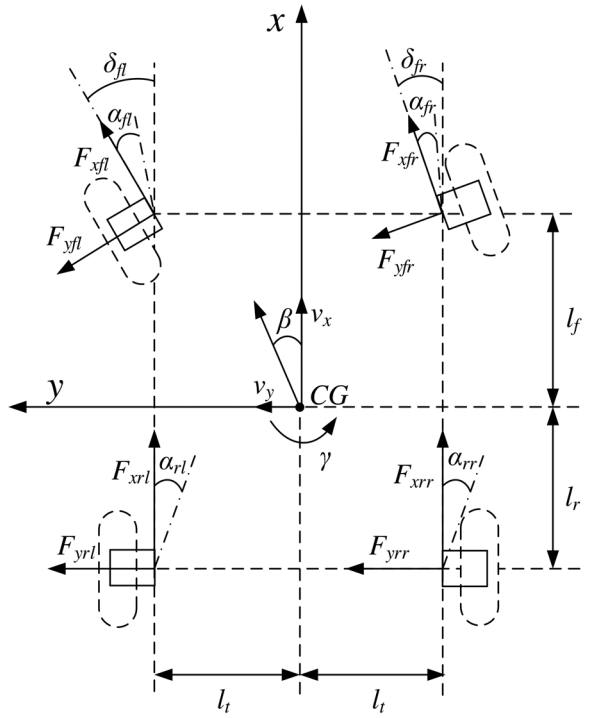

FIGURE 3 Diagram of vehicle body dynamics in the horizontal plane.

roll and pitch displacements, k_{sf} and k_{sr} are the front and rear suspension stiffness, c_{sf} and c_{sr} are the front and rear suspension damping, h_r and h_p are the vertical distances from vehicle centre of gravity (CG) to roll axis and pitch axis, z_{mi} is vertical displacement of each motor, z_i is vertical displacement of vehicle body at each suspension installation corner which is obtained by Equation (11), where i represents fl, fr, rl, rr, which are front left, front right, rear left and rear right, respectively.

$$\begin{cases} z_{fl} = z - l_f\theta + l_t\varphi \\ z_{fr} = z - l_f\theta - l_t\varphi \\ z_{rl} = z + l_r\theta + l_t\varphi \\ z_{rr} = z + l_r\theta - l_t\varphi \end{cases}, \tag{11}$$

where l_t is the half wheel track.

From the horizontal planar motion perspective, motor is rigidly connected to vehicle body through the strut assembly. A diagram is used to describe the vehicle body dynamics in the horizontal plane as shown in Figure 3.

The motor longitudinal and lateral speeds at each corner could be described by vehicle body longitudinal and lateral speeds and yaw rate, as shown in Equation (12):

$$\begin{aligned} v_{xfl} &= (v_x - \dot{\gamma} l_t)\cos\delta_{fl} + (v_y + \dot{\gamma} l_f)\sin\delta_{fl} v_x rl = v_x - \dot{\gamma} l_t \\ v_{xfr} &= (v_x + \dot{\gamma} l_t)\cos\delta_{fr} + (v_y + \dot{\gamma} l_f)\sin\delta_{fr} v_x rr = v_x + \dot{\gamma} l_t \\ v_{yfl} &= (v_y + \dot{\gamma} l_f)\cos\delta_{fl} - (v_x - \dot{\gamma} l_t)\sin\delta_{fl} v_y rl = v_y - \dot{\gamma} l_r \\ v_{yfr} &= (v_y + \dot{\gamma} l_f)\cos\delta_{fr} - (v_x + \dot{\gamma} l_t)\sin\delta_{fr} v_y rr = v_y - \dot{\gamma} l_r \end{aligned}, \tag{12}$$

where v_{xi} and v_{yi} are motor longitudinal and lateral speed, δ_{fl} and δ_{fr} are front left and front right wheel steering angles that satisfy the Ackerman steering principle [37].

The vehicle body dynamics in the horizontal plane are described by Equations (13)–(15):

$$\begin{aligned} m_v\dot{v}_x = {} & F_{xfl}\cos\delta_{fl} + F_{xfr}\cos\delta_{fr} - F_{yfl}\sin\delta_{fl} - F_{yfr}\sin\delta_{fr} \\ & + F_{xrl} + F_{xrr} - F_{res} + m_v\dot{\gamma} v_y - m_v h_p\ddot{\theta}, \end{aligned} \tag{13}$$

$$\begin{aligned} m_v\dot{v}_y = {} & F_{xfl}\sin\delta_{fl} + F_{xfr}\sin\delta_{fr} + F_{yfl}\cos\delta_{fl} + F_{yfr}\cos\delta_{fr} \\ & + F_{yrl} + F_{yrr} - m_v\dot{\gamma} v_x + m_v h_r\ddot{\varphi}, \end{aligned} \tag{14}$$

$$\begin{aligned} I_z\ddot{\gamma} = {} & (F_{xfl}\sin\delta_{fl} + F_{xfr}\sin\delta_{fr} + F_{yfl}\cos\delta_{fl} + F_{yfr}\cos\delta_{fr})l_f \\ & - (F_{yrl} + F_{yrr})l_r + (F_{xfr}\cos\delta_{fr} - F_{xfl}\cos\delta_{fl} \\ & + F_{yfl}\sin\delta_{fl} - F_{yfr}\sin\delta_{fr} - F_{xrl} + F_{xrr})l_t, \end{aligned} \tag{15}$$

where I_z is the vehicle body yaw inertia, F_{xi} and F_{yi} are longitudinal and lateral forces acting on vehicle body, F_{res} is vehicle resistance. The values of vehicle body and suspension parameters are listed in Table 1 [36].

3.2 | Tyre dynamic modelling

In the wheel, motor is rigidly installed on the wheel rim which is connected to tyre carcass. The rigid ring tyre model is adopted to describe the tyre force, as shown in Figure 4 [20, 21]. In this model, the tyre carcass which connects the rim and tyre surface is represented by translational and rotational springs and dampers. The tyre surface is simplified as a rigid ring which contacts with road and generates force and torques.

Based on the rigid ring model, the dynamic equations of the motor and tyre ring are developed. For the motor, in addition to the force and torque from tyre carcass, it also bears the force and torque from the strut assembly and suspension. The motor dynamics are described by the following equations:

$$m_m\ddot{x}_m = k_x(x_r - x_m) + c_x(\dot{x}_r - \dot{x}_m) - c_x\dot{\theta}_m(z_r - z_m) - F_x, \tag{16}$$

$$m_m\ddot{y}_m = k_y(y_r - y_m) + c_y(\dot{y}_r - \dot{y}_m) - F_y, \tag{17}$$

$$m_m\ddot{z}_m = k_z(z_r - z_m) + c_z(\dot{z}_r - \dot{z}_m) + c_z\dot{\theta}_m(x_r - x_m) - F_z, \tag{18}$$

$$\begin{aligned} I_{mx}\ddot{\varphi}_m = {} & k_\varphi(\varphi_r - \varphi_m) + c_\varphi(\dot{\varphi}_r - \dot{\varphi}_m) \\ & - c_\varphi\dot{\theta}_r(\gamma_r - \gamma_m) - I_{ry}\dot{\theta}_r\dot{\gamma}_r + T_p, \end{aligned} \tag{19}$$

$$I_{my}\ddot{\theta}_m = k_\theta(\theta_r - \theta_m) + c_\theta(\dot{\theta}_r - \dot{\theta}_m) + T_m, \tag{20}$$

TABLE 1 Values of vehicle body and suspension parameters.

Parameter	Description	Value	Parameter	Description	Value
m_v	Vehicle body mass	1320 kg	k_{sf}	Front suspension stiffness	16100 N/m
I_x	Vehicle body roll inertia	580 kg·m^2	k_{sr}	Rear suspension stiffness	35200 N/m
I_y	Vehicle body pitch inertia	1910 kg·m^2	c_{sf}	Front suspension damping	2150 N·s/m
I_z	Vehicle body yaw inertia	2030 kg·m^2	c_{sr}	Rear suspension damping	2980 N·s/m
h_r	Vertical distances of vehicle CG to roll axis	0.35 m	h_p	Vertical distances of vehicle CG to pitch axis	0.35 m
l_f	Front wheelbase	1.13 m	l_r	Rear wheelbase	1.69 m
l_t	Half wheel track	0.767 m			

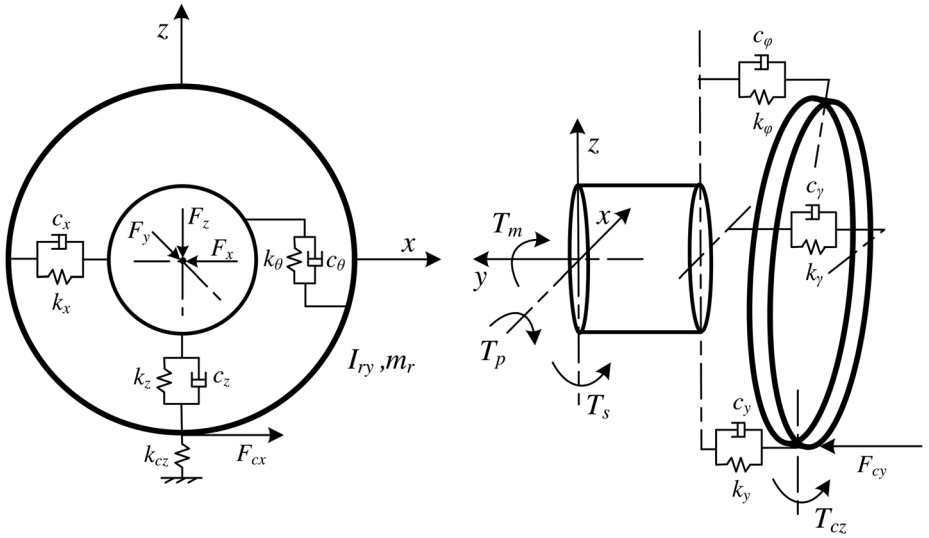

FIGURE 4 Rigid ring tyre model.

$$I_{mz}\ddot{\gamma}_m = k_\gamma(\gamma_r - \gamma_m) + c_\gamma(\dot{\gamma}_r - \dot{\gamma}_m) + c_\gamma\dot{\theta}_r(\varphi_r - \varphi_m) + I_{ry}\dot{\theta}_r\dot{\varphi}_r + T_s. \quad (21)$$

For the rigid ring which represents the tyre surface, it moves under the force and torque from the tire carcass and road:

$$m_r\ddot{x}_r = -k_x(x_r - x_m) - c_x(\dot{x}_r - \dot{x}_m) + c_x\dot{\theta}_m(z_r - z_m) + F_{cx}, \quad (22)$$

$$m_r\ddot{y}_r = -k_y(y_r - y_m) - c_y(\dot{y}_r - \dot{y}_m) + F_{cy}, \quad (23)$$

$$m_r\ddot{z}_r = -k_z(z_r - z_m) - c_z(\dot{z}_r - \dot{z}_m) - c_z\dot{\theta}_m(x_r - x_m) + F_{cz}, \quad (24)$$

$$I_{rx}\ddot{\varphi}_r = (y_r - y_m - r_l\varphi_r)F_{cz} - k_\varphi(\varphi_r - \varphi_m) - c_\varphi(\dot{\varphi}_r - \dot{\varphi}_m) + c_\varphi\dot{\theta}_r(\gamma_r - \gamma_m) + I_{ry}\dot{\theta}_r\dot{\gamma}_r - r_lF_{cy}, \quad (25)$$

$$I_{ry}\ddot{\theta}_r = -k_\theta(\theta_r - \theta_m) - c_\theta(\dot{\theta}_r - \dot{\theta}_m) - F_{cx}r_e, \quad (26)$$

$$I_{rz}\ddot{\gamma}_r = -k_\gamma(\gamma_r - \gamma_m) - c_\gamma(\dot{\gamma}_r - \dot{\gamma}_m) - c_\gamma\dot{\theta}_r(\varphi_r - \varphi_m) - I_{ry}\dot{\theta}_r\dot{\varphi}_r + T_{cz}, \quad (27)$$

where m_m is the motor mass, I_{mx}, I_{my}, I_{mz} are the motor inertia about its longitudinal, lateral and vertical axes, m_r is the tyre ring mass, I_{rx}, I_{ry}, I_{rz} are the tyre ring inertia about its longitudinal, lateral and vertical axes, x_m, y_m, z_m are the motor longitudinal, lateral and vertical displacements, φ_m,θ_m,γ_m are motor rotational displacements about its longitudinal, lateral and vertical rotational axes, x_r, y_r, z_r are tyre ring longitudinal, lateral and vertical displacements, φ_r, θ_r, γ_r are tyre ring rotational displacements about its longitudinal, lateral and vertical rotational axes, k_x, k_y, k_z are the tyre longitudinal, lateral and vertical stiffness, k_φ, k_θ, k_γ are the tyre rotational stiffness about its longitudinal, lateral and vertical axes, c_x, c_y, c_z are the tyre longitudinal, lateral and vertical damping, c_φ, c_θ, c_γ are the tyre rotational damping about its longitudinal, lateral and vertical axes, F_x, F_y, F_z are the forces applied on motor from vehicle body and suspension. T_p is the torque applied on motor about its longitudinal axis, T_m is the motor torque, T_s is the torque from the steering system, F_{cx}, F_{cy}, F_{cz} are longitudinal, lateral and vertical tyre road

TABLE 2 Values of motor and tyre parameters

Parameter	Description	Value	Parameter	Description	Value
m_m	Motor mass	67 kg	m_r	Ring mass	7.18 kg
I_{mx}, I_{mz}	Motor inertia about its longitudinal and vertical axes	6 kg·m^2	I_{rx}, I_{rz}	Ring inertia about its longitudinal and vertical axes	0.326 kg·m^2
I_{my}	Motor inertia about its lateral axis	1.01 kg·m^2	I_{ry}	Ring inertia about its lateral axis	0.636 kg·m^2
k_x, k_z	Tyre longitudinal and vertical stiffness	1.57e6 N/m	k_φ,k_γ	Tyre rotational stiffness about its longitudinal and vertical axes	2.2e4 Nm/rad
k_y	Tyre lateral stiffness	5.11e5 N/m	k_θ	Tyre rotational stiffness about its lateral axis	7.7e4 Nm/rad
c_x, c_z	Tyre longitudinal and vertical damping	320 N·s/m	c_φ, c_γ	Tyre rotational damping about its longitudinal and vertical axes	8 Nm·s /rad
c_y	Tyre lateral damping	120 N·s/m	c_θ	Tyre rotational damping about its lateral axis	50 Nm·s /rad
r_l	Tyre loaded radius	0.29 m	k_{px}	Tyre longitudinal tread stiffness	17e6 N/m
r_e	Tyre effective radius	0.3029 m	k_{py}	Tyre lateral tread stiffness	13e6 N/m
μ	Tyre road friction coefficient	0.9	k_{cy}	Tyre lateral residual stiffness	6e5 N/m
A	Half tyre road contact length	0.0534 m	k_{cz}	Tyre vertical residual stiffness	2.25e5 N/m

contact forces, T_{cz} is the tyre aligning moment, r_l is the tyre loaded radius.

For tyre road contact force, the vertical force is described by a residual stiffness k_{cz} as shown in Equation (28):

$$F_{cz} = -k_{cz} z_r. \tag{28}$$

The longitudinal force, lateral force and aligning moment generated by tyre road contact are described by the brush model which treats longitudinal and lateral forces separately here when tyre force is not saturated [20, 38], as shown in Equations (29)–(31):

$$F_{cx} = \begin{cases} \mu F_{cz}\left\{3|\lambda_x\zeta_{cx}| - 3|\lambda_x\zeta_{cx}|^2 + |\lambda_x\zeta_{cx}|^3\right\}\mathrm{sgn}(\zeta_{cx}) & |\zeta_{cx}| \le 1/\lambda_x \\ \mu F_{cz}\mathrm{sgn}(\zeta_{cx}) & |\zeta_{cx}| > 1/\lambda_x \end{cases}, \tag{29}$$

$$F_{cy} = \begin{cases} \mu F_{cz}\left\{3|\lambda_y\zeta_{cy}| - 3|\lambda_y\zeta_{cy}|^2 + |\lambda_y\zeta_{cy}|^3\right\}\mathrm{sgn}(\zeta_{cy}) & |\zeta_{cy}| \le 1/\lambda_y \\ \mu F_{cz}\mathrm{sgn}(\zeta_{cy}) & |\zeta_{cy}| > 1/\lambda_y \end{cases}, \tag{30}$$

$$T_{cz} = \begin{cases} \mu F_{cz} a|\lambda_y\zeta_{cy}|\left(1 - |\lambda_y\zeta_{cy}|\right)^3\mathrm{sgn}(\zeta_{cy}) & |\zeta_{cy}| \le 1/\lambda_y \\ 0 & |\zeta_{cy}| > 1/\lambda_y \end{cases}, \tag{31}$$

where μ is the tyre road friction coefficient, a is the half tyre road contact length, ζ_{cx} and ζ_{cy} are tyre longitudinal and lateral slip ratios. Parameters λ_x and λ_y are defined as:

$$\lambda_x = \frac{2k_{px}a^2}{3\mu F_{cz}}, \lambda_y = \frac{2k_{py}a^2}{3\mu F_{cz}}, \tag{32}$$

where k_{px} and k_{py} are the tyre longitudinal and lateral tread stiffness.

In tyre-road interaction, when FWS or DMT control inputs change, it needs time for tyre carcass and tyre-road contact to reach another steady-state condition, which is represented by the relaxation length. The dynamic process of tyre slip ratio and slip angle changes are described by the following first order equations:

$$\begin{aligned} \sigma_{cx}\dot{\zeta}_{cx} + |r_e\dot{\theta}_r|\zeta_{cx} + \dot{x}_r - r_e\dot{\theta}_r = 0 \\ \sigma_{cy}\dot{\zeta}_{cy} + |r_e\dot{\theta}_r|\zeta_{cy} + \dot{y}_r - r_l\dot{\varphi}_r = 0 \end{aligned}. \tag{33}$$

The longitudinal relaxation length σ_{cx} and lateral relaxation length σ_{cy} are defined as:

$$\sigma_{cx} = \frac{1}{2k_{px}a}\frac{\partial F_{cx}}{\partial \zeta_{cx}}, \sigma_{cy} = \left[\frac{1}{2k_{py}a} + \frac{1}{k_{cy}}\right]\frac{\partial F_{cy}}{\partial \zeta_{cy}}, \tag{34}$$

where k_{cy} is the tyre lateral residual stiffness.

The values of motor and tyre parameters are shown in Table 2.

4 | VEHICLE DYNAMIC RESPONSE TO DMT AND FWS INPUTS

In the autonomous vehicle with in-wheel motor, the yaw moment and lateral force generated by DMT and FWS are used to control the vehicle dynamics. In this section, the dynamic response of the bicycle model and detailed model are compared with the same DMT and FWS inputs. The vehicle models are built with the help of the Matlab/Simulink software platform. In the simulation models, the PID controller is used to achieve

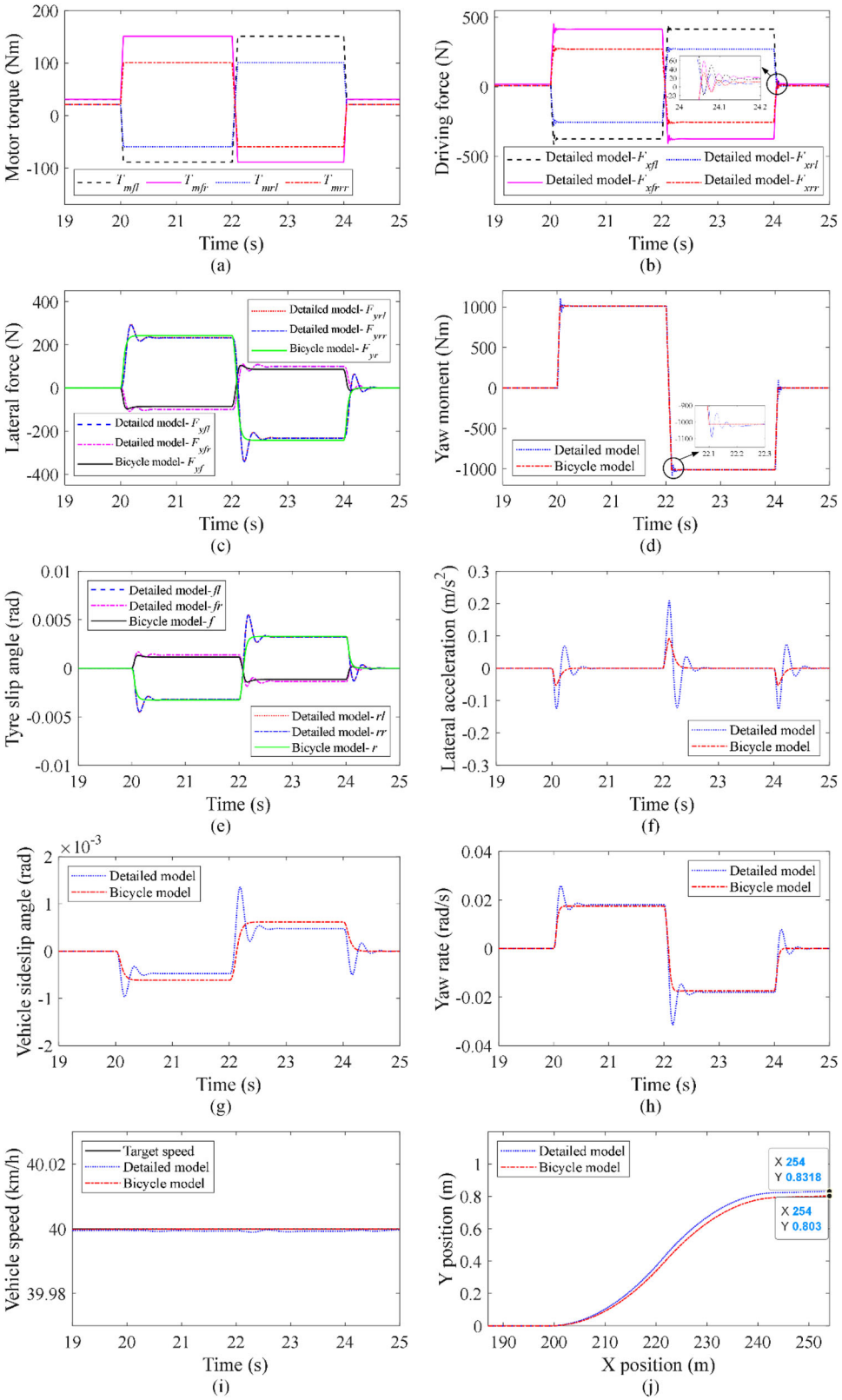

FIGURE 5 Vehicle dynamic response to DMT input at 40 km/h.

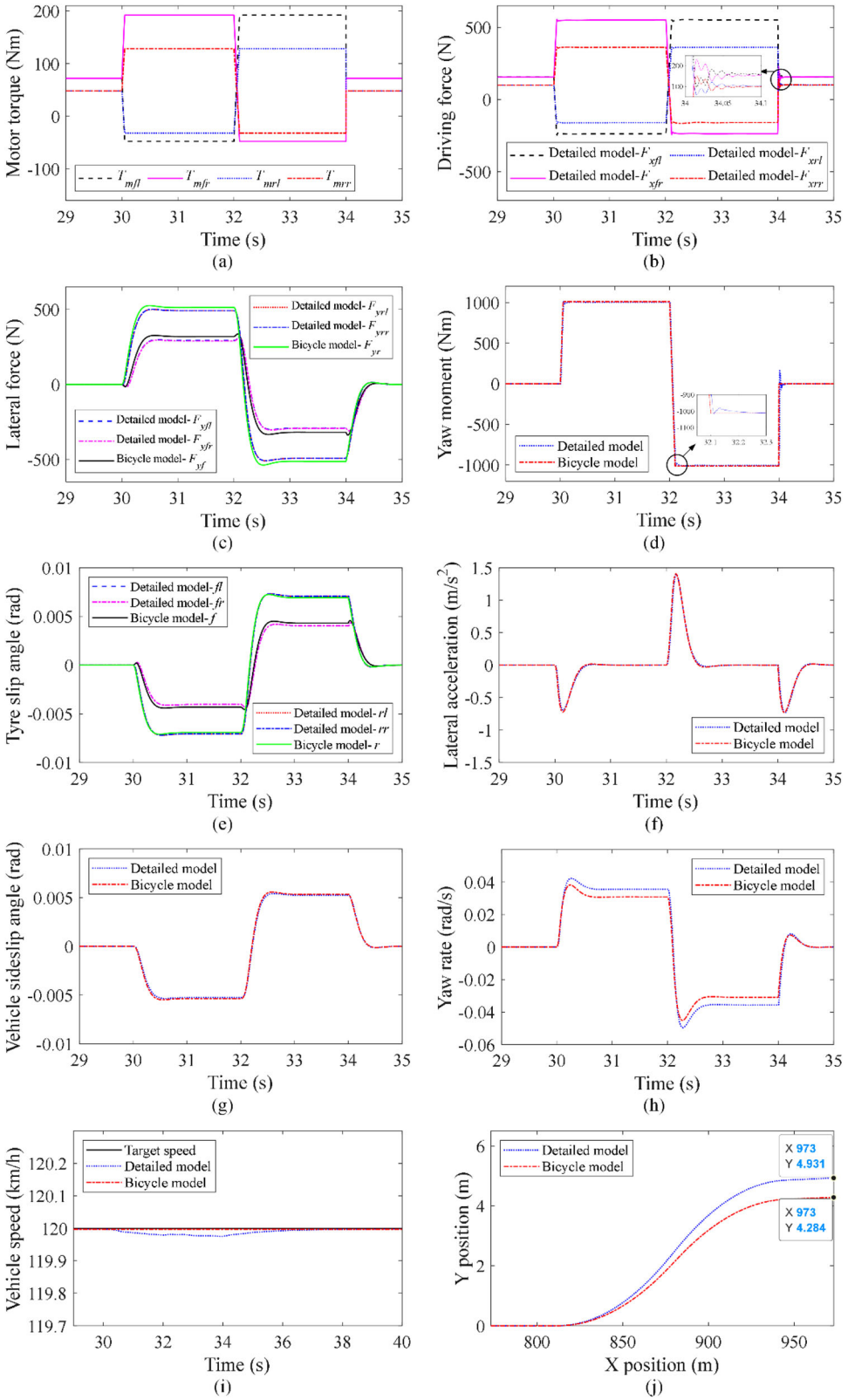

FIGURE 6 Vehicle dynamic response to DMT input at 120 km/h.

the target vehicle speed, in which the vehicle speed error and its integration and derivative are taken as the input of the PID controller. The PID controller output is the required longitudinal force:

$$u = k_p(v_{xdes} - v_x) + \int k_i(v_{xdes} - v_x) + k_d(\dot{v}_{xdes} - \dot{v}_x), \quad (35)$$

where v_{xdes} is the desired vehicle speed, k_p, k_i and k_d are the proportional, integral and derivative coefficients.

The driving force is allocated to each wheel according to the wheel vertical load to evenly use each tyre-road friction. Therefore, the motor torque at each wheel is:

$$T_{mfl} = T_{mfr} = \frac{ul_r r_e}{2(l_f + l_r)}, T_{mrl} = T_{mrr} = \frac{ul_f r_e}{2(l_f + l_r)}. \quad (36)$$

4.1 | Vehicle dynamic response to DMT input

In the DMT input response analysis, a DMT between left and right motors is implemented to generate a yaw moment on vehicle. The DMT is generated by changing the right side motor torque and the left side motor torque with the same value but in opposite directions. Thus, only yaw moment is generated while the longitudinal driving force is unchanged. Regarding the front and rear side allocation, considering the maximum tyre-road friction force is proportional to the vertical load, it is allocated according to the vehicle mass distribution to exploit the tyre-road contact force equally. In the bicycle model, the DMT is transformed into yaw moment and works on vehicle body directly. In the detailed model, motor torque firstly acts on the tyre carcass, causing tyre deformation and tyre surface slip. Then longitudinal force is generated between tyre and road. The longitudinal force is transferred to vehicle body via the tyre ring, tyre carcass, motor and strut assembly. It could be found in the detailed model, motor torque is transformed into yaw moment through a long route introduced by tyre. The simulation results of the two models' response to DMT input are illustrated in Figures 5 and 6 with the vehicle speed at 40 km/h and 120 km/h, respectively.

In Figures 5g and 5h, it could be seen that the vehicle sideslip angle and yaw rate in detailed model show remarkable fluctuations with the DMT change, while in the bicycle model the vehicle sideslip and yaw rate change very smoothly, which demonstrates that the detailed model presents more transient process than bicycle model. The lateral force and yaw moment acting on vehicle body are shown in Figures 5c and 5d. When motor torque changes, the driving force also changes to the new steady-state value through a transient process due to tyre dynamics. Figure 5b shows the vibrating vehicle longitudinal driving force from each wheel in detailed model which is the fundamental reason for different vehicle body movements. Vehicle speed comparison is shown in Figure 5i in which the detailed model shows speed vibration caused by driving force fluctuation while the bicycle model does not show any speed vibration because all DMT just cancel each other. Figure 5j shows the vehicle path under the same DMT inputs. There is a 3.59% lateral offset between two models.

Figure 6 shows the vehicle dynamic response to DMT input at 120 km/h. In this high vehicle speed scenario, when the same DMT is applied, the vehicle lateral force is much larger than in the low vehicle speed scenario, indicating a more aggressive vehicle movement. The transient process in detailed model is not obvious compared with the bicycle model since the sideslip and yaw rate in the detailed model do not show clear fluctuations. Actually, driving force and yaw moment fluctuations still exist due to the tyre dynamics, as shown in Figures 6b and 6d. However, in a high vehicle speed scenario, the vehicle sideslip angle and yaw rate change to larger steady-state values in a longer time, so the transient vibrations are immersed in the changing process.

Although transient vibrations are not evident in the high-speed scenario, steady-state errors of vehicle sideslip angle and yaw rate are increased, demonstrated by the 15.1% lateral offset between detailed model and bicycle model as shown in Figure 6j. The reason is that in the bicycle model, the tyre cornering stiffness is assumed as a constant value while the real tyre cornering stiffness changes with its slip angle. In high vehicle speed scenario, large tyre slip angle results in more cornering stiffness and lateral force errors.

4.2 | Vehicle dynamic response to FWS input

The vehicle dynamics response to FWS input is shown in Figures 7 and 8 with vehicle speed at 40 km/h and 120 km/h, respectively. A sinusoidal FWS input is implemented on two models. Because the steering angle is gradually increased and no impulsive force is applied to vehicle, vehicle transient vibration in the detailed model is avoided, illustrated by the smooth vehicle sideslip angle and yaw rate. When vehicle speed is 40 km/h, the vehicle lateral force caused by steering input is relatively small so there is not a significant difference in tyre cornering stiffness. The very close vehicle path shown in Figure 7h proves the validity of bicycle model for vehicle lateral dynamic control research in mild and moderate driving condition. In contrast, Figure 8 shows a significant path difference between two models when vehicle speed is higher. The obvious lateral force difference in Figure 8b indicates the different tyre cornering stiffness, resulting in a 3.43% offset between two models.

5 | PATH FOLLOWING CONTROL STRATEGY DESIGN

From the vehicle dynamic response analysis, tyre dynamics cause significant transient vibrations on vehicle body and steady-state error on vehicle path, depending on driving conditions. Therefore, the bicycle model has limitations to describe the vehicle transient response to fast torque and

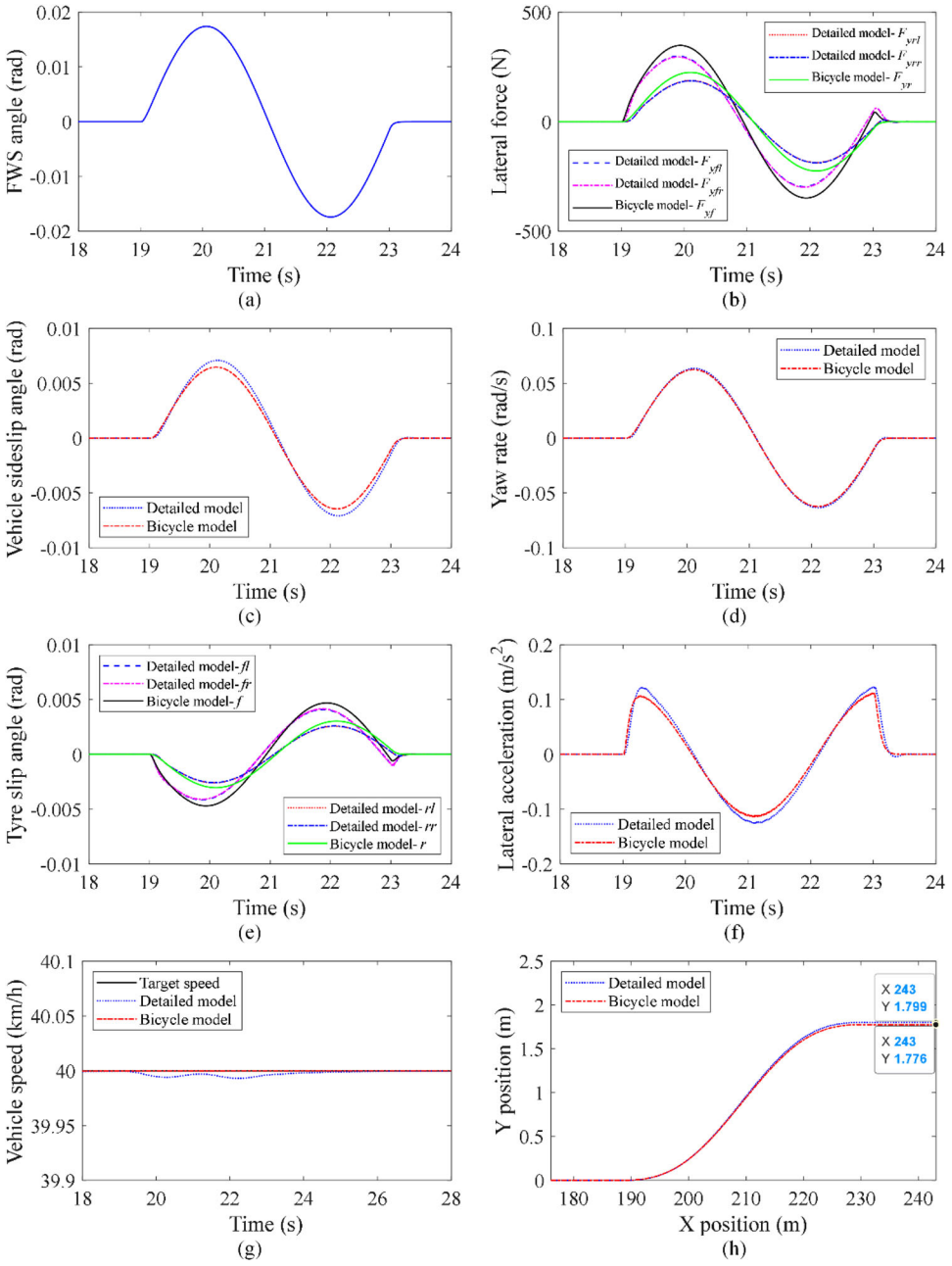

FIGURE 7 Vehicle dynamic response to FWS input at 40 km/h.

force changes. Furthermore, even if the torque and force are smoothly applied and the transient vibration is avoided, the assumption of rigid tyre carcass and constant tyre parameter value still generates steady-state error under large tyre forces.

Since the bicycle model is normally used for vehicle dynamic control research rather than just vehicle dynamic analysis, the two vehicle models are compared during vehicle path following control. As shown in Figure 9 [39, 40], the vehicle path following modelling and control strategy design is based on the bicycle model.

To design the path following control strategy, the state variables X and control variables U are chosen as:

$$X = [e, \dot{e}, \Delta\gamma, \Delta\dot{\gamma}]^T, U = [\delta, M_\gamma]^T, \tag{37}$$

where e is the path offset which is the closest distance from the vehicle CG to the desired path. On the desired path, the point closest to vehicle CG is defined as point O. $\Delta\gamma$ is the heading angle error which is the error between vehicle longitudinal axis and the tangent of the desired path at point O. The control target is to reduce the path offset and heading angle error to 0.

FIGURE 8 Vehicle dynamic response to FWS input at 120 km/h.

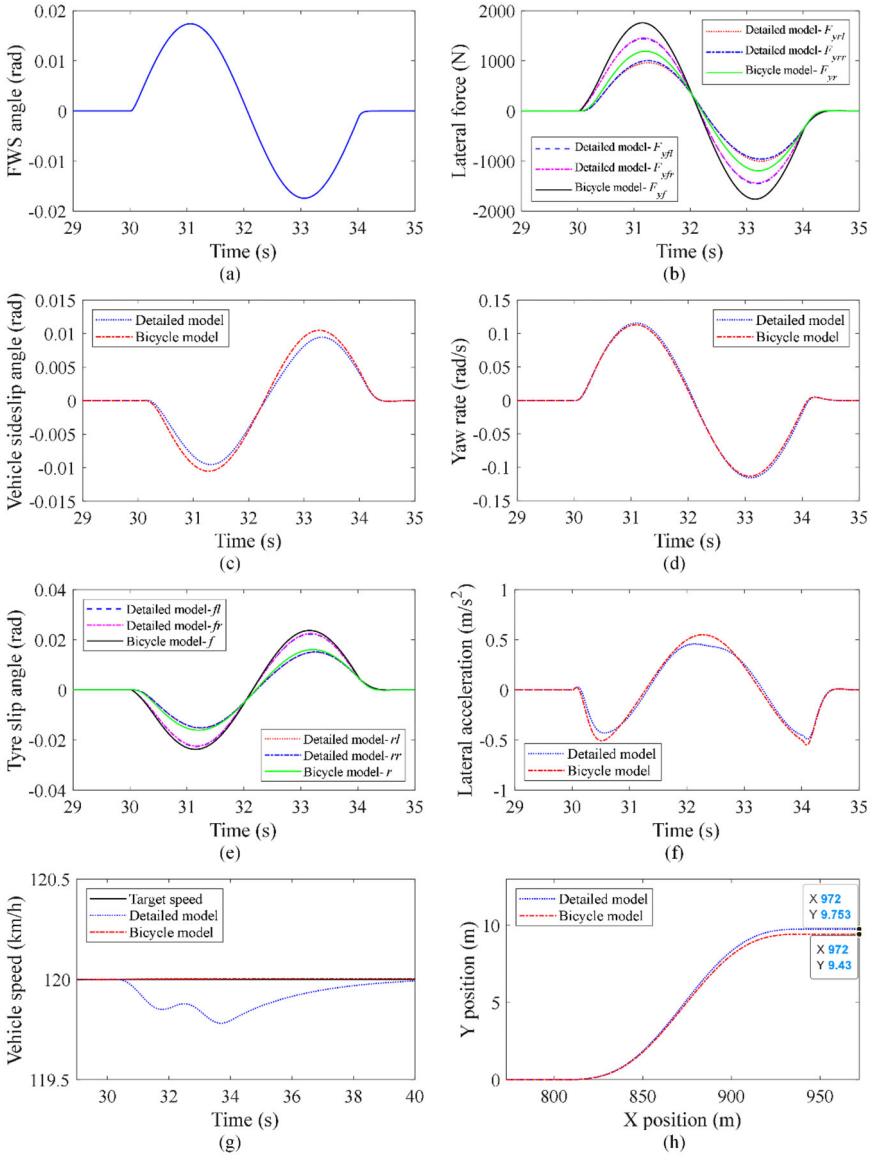

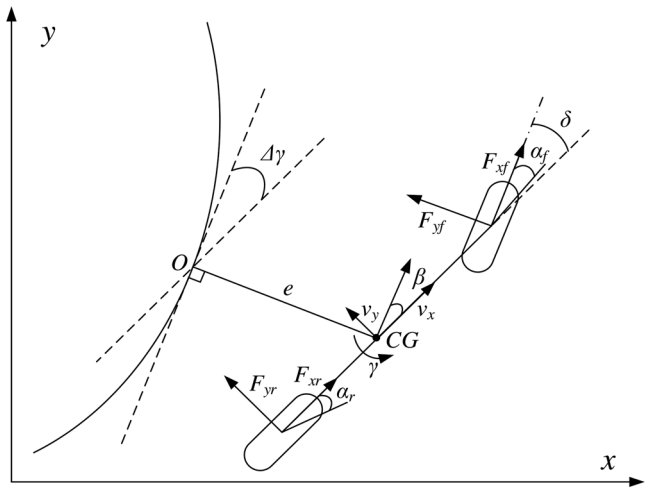

FIGURE 9 Vehicle path following control modelling.

The path offset and heading angle error changing rates are described as:

$$\begin{aligned} \dot{e} &= v_y \cos(\Delta\gamma) + v_x \sin(\Delta\gamma) \\ \Delta\dot{\gamma} &= \dot{\gamma} - \dot{\gamma}_{des} = \dot{\gamma} - \kappa v_x \end{aligned}, \tag{38}$$

where κ is the desired path curvature at point O.

Under small angle assumption and constant vehicle longitudinal speed [41], the path offset changing rate is simplified as:

$$\dot{e} = v_y + v_x \Delta\gamma. \tag{39}$$

The second order derivative of path offset and heading angle error is deduced as Equation (40):

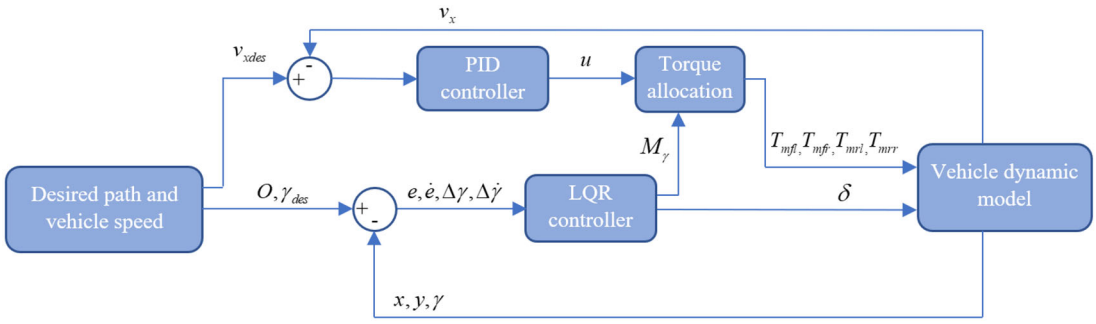

FIGURE 10 Flowchart of vehicle path following control.

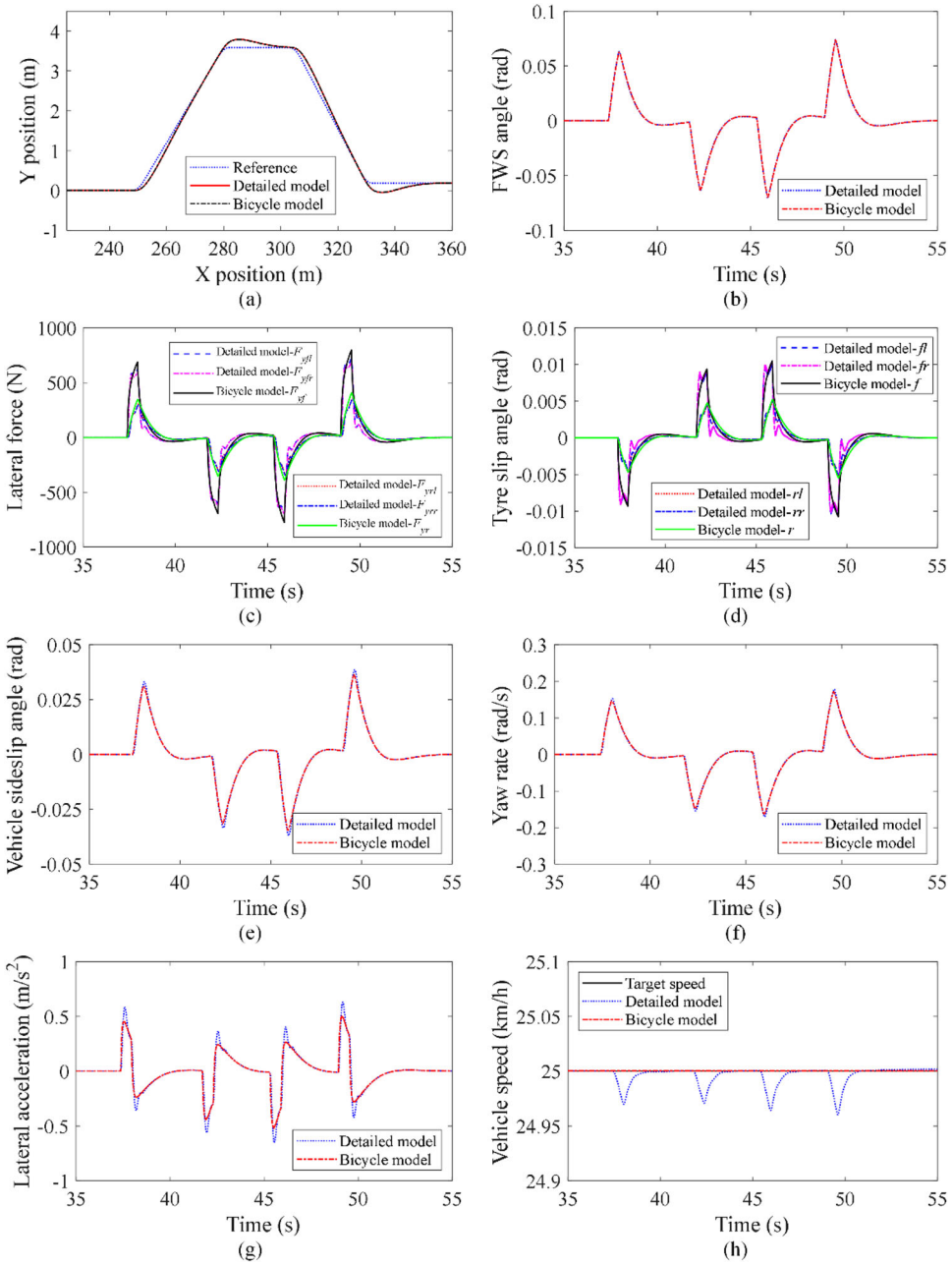

FIGURE 11 Vehicle path following control with only FWS at 25 km/h.

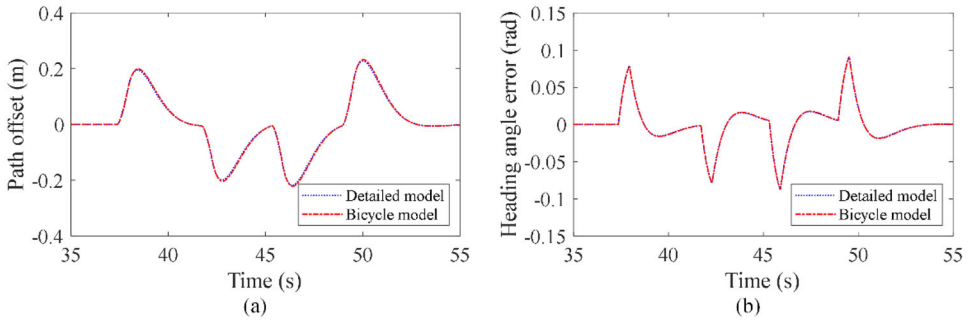

FIGURE 12 Vehicle path following error with only FWS at 25 km/h.

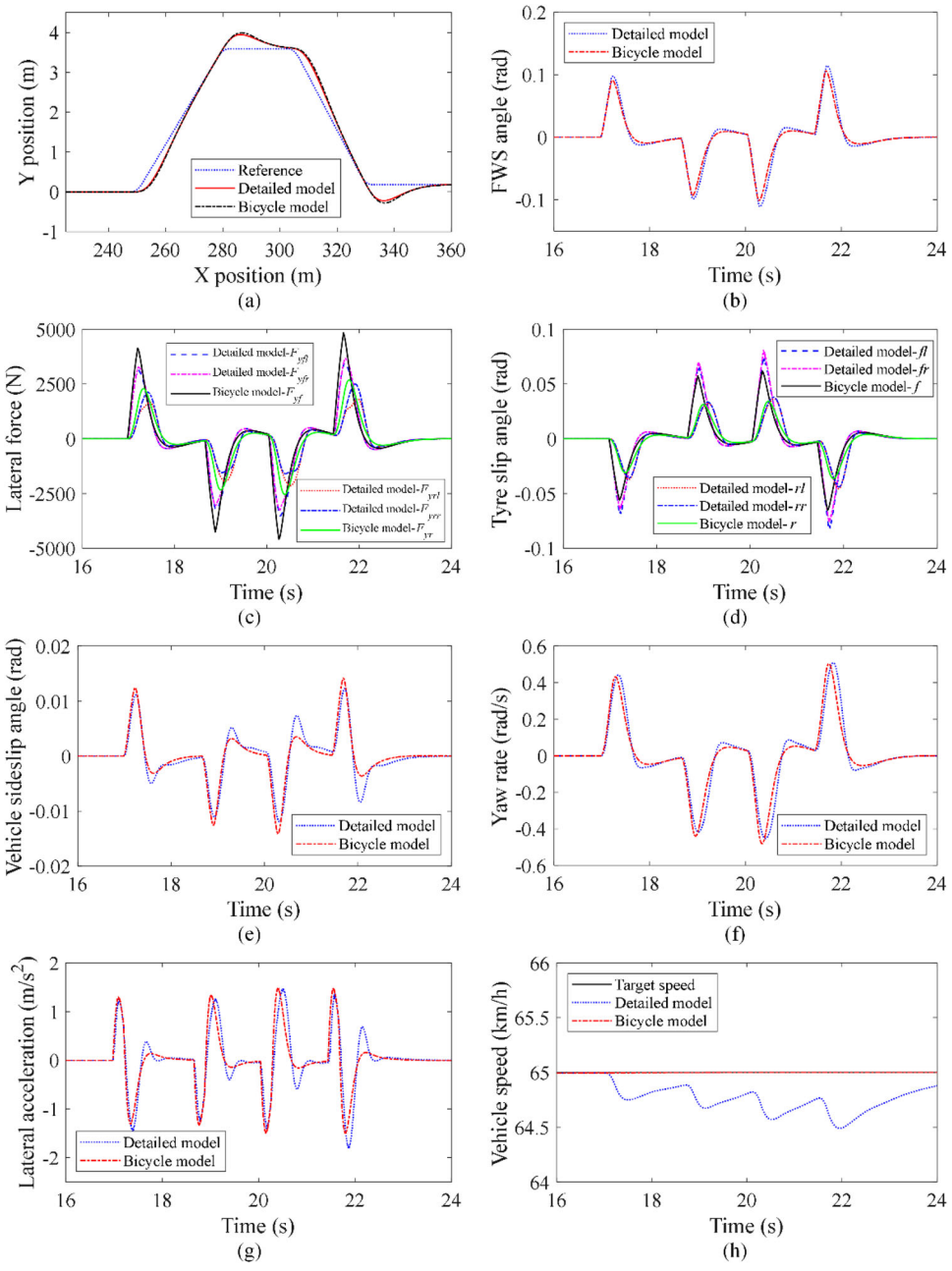

FIGURE 13 Vehicle path following control with only FWS at 65 km/h.

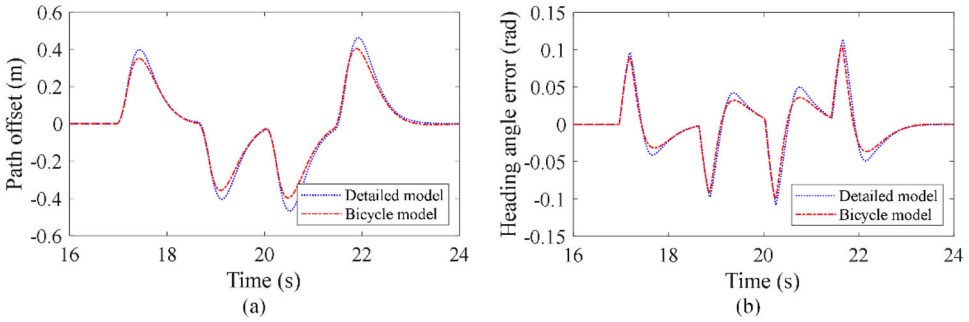

FIGURE 14 Vehicle path following error with only FWS at 65 km/h.

$$\begin{aligned}\ddot{e} &= \dot{v}_y + v_x\Delta\dot{\gamma}\\ \Delta\ddot{\gamma} &= \ddot{\gamma} - \dot{\kappa}v_x\end{aligned}. \tag{40}$$

Based on the vehicle bicycle model described by Equations (2), (4), (5), (38) and (40), Equation (41) could be obtained:

$$\begin{aligned}\ddot{e} &= -\frac{2c_f\left(\beta-\delta+\frac{l_f\dot{\gamma}}{v_x}\right)}{m_g} - \frac{2c_r\left(\beta-\frac{l_r\dot{\gamma}}{v_x}\right)}{m_g} - \dot{\gamma}v_x + v_x\Delta\dot{\gamma}\\ &= -\frac{2c_f\left(\frac{v_y}{v_x}-\delta+\frac{l_f(\Delta\dot{\gamma}+\kappa v_x)}{v_x}\right)}{m_g} - \frac{2c_r\left(\frac{v_y}{v_x}-\frac{l_r(\Delta\dot{\gamma}+\kappa v_x)}{v_x}\right)}{m_g}\\ &\quad -(\Delta\dot{\gamma}+\kappa v_x)v_x + v_x\Delta\dot{\gamma}\\ &= -\frac{2c_f\left(\frac{\dot{e}-v_x\Delta\gamma}{v_x}-\delta+\frac{l_f(\Delta\dot{\gamma}+\kappa v_x)}{v_x}\right)}{m_g}\\ &\quad -\frac{2c_r\left(\frac{\dot{e}-v_x\Delta\gamma}{v_x}-\frac{l_r(\Delta\dot{\gamma}+\kappa v_x)}{v_x}\right)}{m_g} - \kappa v_x^2\end{aligned}. \tag{41}$$

Based on the vehicle bicycle model described by Equations (3), (4), (5), (38) and (40), Equation (42) could be obtained:

$$\begin{aligned}\Delta\ddot{\gamma} &= -\frac{2c_f\left(\beta-\delta+\frac{l_f\dot{\gamma}}{v_x}\right)l_f}{I_{zg}} + \frac{2c_r\left(\beta-\frac{l_r\dot{\gamma}}{v_x}\right)l_r}{I_{zg}} + \frac{M_r}{I_{zg}} - v_x\dot{\kappa}\\ &= -\frac{2c_f\left(\frac{v_y}{v_x}-\delta+\frac{l_f(\Delta\dot{\gamma}+\kappa v_x)}{v_x}\right)l_f}{I_{zg}} + \frac{2c_r\left(\frac{v_y}{v_x}-\frac{l_r(\Delta\dot{\gamma}+\kappa v_x)}{v_x}\right)l_r}{I_{zg}} + \frac{M_r}{I_{zg}} - v_x\dot{\kappa}\\ &= -\frac{2c_f\left(\frac{\dot{e}-v_x\Delta\gamma}{v_x}-\delta+\frac{l_f(\Delta\dot{\gamma}+\kappa v_x)}{v_x}\right)l_f}{I_{zg}} + \frac{2c_r\left(\frac{\dot{e}-v_x\Delta\gamma}{v_x}-\frac{l_r(\Delta\dot{\gamma}+\kappa v_x)}{v_x}\right)l_r}{I_{zg}}\end{aligned}. \tag{42}$$

Rearrange Equations (41) and (42) according to the state variables and control variables, the following state space equations are obtained:

$$\dot{X} = AX + BU + CW, \tag{43}$$

$$A = \begin{bmatrix} 0 & 1 & 0 & 0\\ 0 & -\frac{2c_f+2c_r}{m_g v_x} & \frac{2c_f+2c_r}{m_g} & \frac{2c_r l_r - 2c_f l_f}{m_g v_x}\\ 0 & 0 & 0 & 1\\ 0 & \frac{2c_r l_r - 2c_f l_f}{I_{zg} v_x} & \frac{2c_f l_f - 2c_r l_r}{I_{zg}} & -\frac{2c_f l_f^2 + 2c_r l_r^2}{I_{zg} v_x} \end{bmatrix},$$

$$B = \begin{bmatrix} 0 & 0\\ \frac{2c_f}{m_g} & 0\\ 0 & 0\\ \frac{2c_f l_f}{I_{zg}} & \frac{1}{I_{zg}} \end{bmatrix}, C = \begin{bmatrix} 0 & 0\\ \frac{2c_r l_r - 2c_f l_f}{m_g} - v_x^2 & 0\\ 0 & 0\\ -\frac{2c_f l_f^2 + 2c_r l_r^2}{I_{zg}} & -v_x \end{bmatrix}, W = \begin{bmatrix}\kappa\\ \dot{\kappa}\end{bmatrix}. \tag{44}$$

The state space equation describes how the vehicle state changes with the control input. The LQR control is adopted to design the feedback control strategy which uses FWS and DMT to eliminate the path offset and heading angle errors. The target of LQR control is to minimize the cost function J in the following equation:

$$J = \int_0^\infty (X^T QX + U^T RU)dt, \tag{45}$$

where Q and R are weighting matrices representing the intentions of reducing the corresponding variables. Larger matrix elements mean stronger intentions to reduce the corresponding variables. When the weighting matrix elements are selected as Equation (46), Equation (45) is rewritten as Equation (47) which more clearly shows the compromise among reducing path following errors and restricting the control inputs.

$$Q = diag[q_{11}, q_{22}, q_{33}, q_{44}], R = diag[r_{11}, r_{22}], \tag{46}$$

$$J = \int_0^\infty (q_{11}e^2 + q_{22}\dot{e}^2 + q_{33}\Delta\gamma^2 + q_{44}\Delta\dot{\gamma}^2 + r_{11}\delta^2 + r_{22}M_r^2)dt. \tag{47}$$

In Equation (45), $q_{11}e^2$ represents the intention to reduce the path offset e, $q_{22}\dot{e}^2$ represents the intention to limit the changing

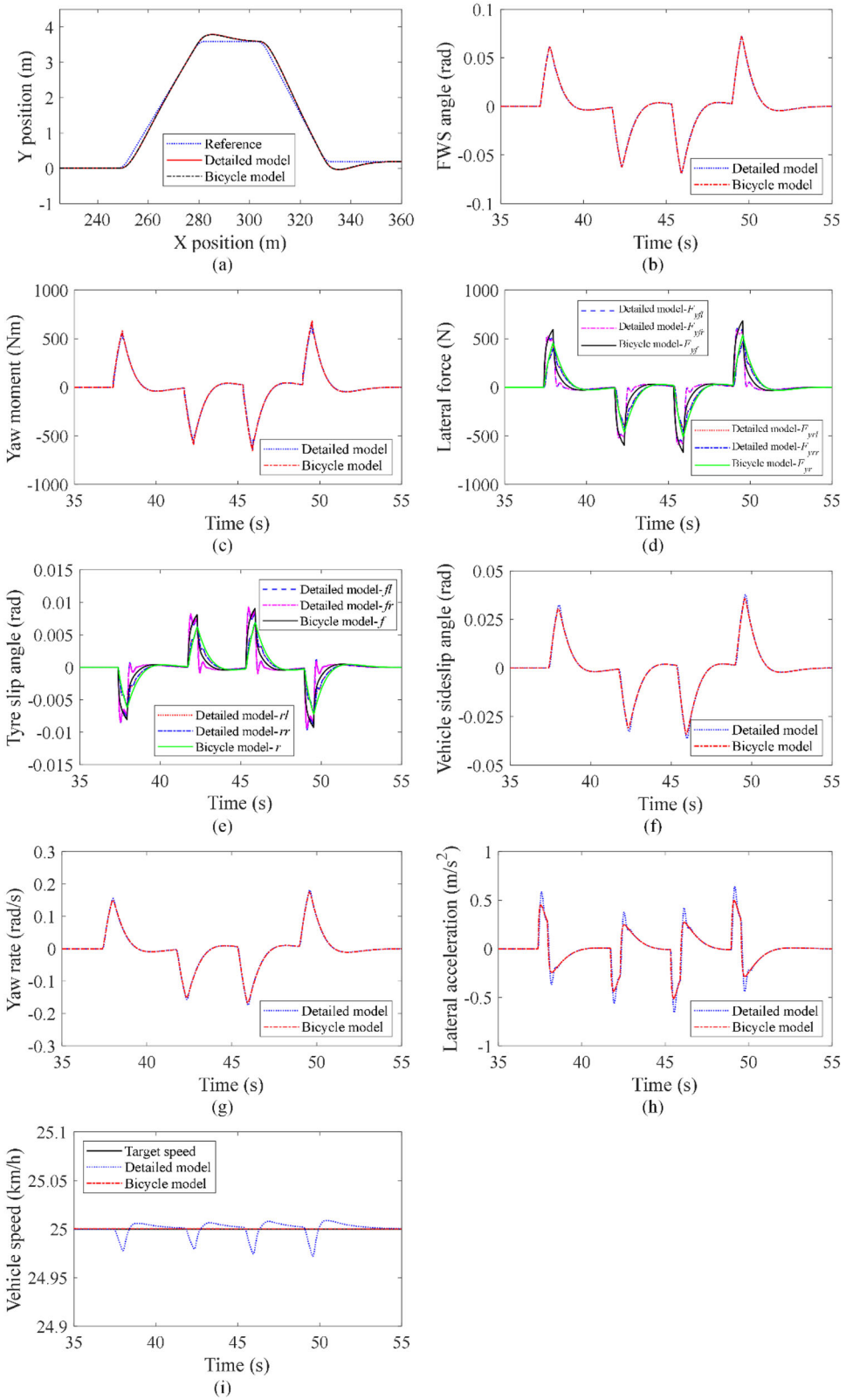

FIGURE 15 Vehicle path following control with combined FWS and DMT at 25 km/h.

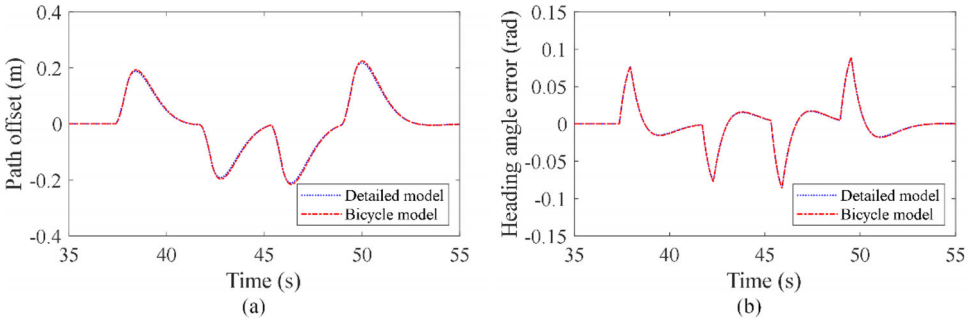

FIGURE 16 Vehicle path following error with combined FWS and DMT at 25 km/h.

rate of path offset e, $q_{33}\Delta\gamma^2$ represents the intention to reduce the heading angle error, $q_{44}\Delta\dot{\gamma}^2$ represents the intention to limit the changing rate of heading angle error, $r_{11}\delta^2$ represents the intention to restrict the FWS control input, $r_{22}M_r^2$ represents the intention to restrict the DMT control input. When elements in Q are increased, it represents smaller errors and errors changing rates are demanded. Accordingly, larger control inputs would be required. As contrast, when elements in R are increased, it represents smaller control inputs can be applied, which might result in larger errors and worse control effects. The LQR parameters should be selected to achieve a balance between control targets and control inputs. In this research, Q and R are selected as:

$$Q = \begin{bmatrix} 60 & 0 & 0 & 0 \\ 0 & 3 & 0 & 0 \\ 0 & 0 & 60 & 0 \\ 0 & 0 & 0 & 3 \end{bmatrix}, \; R = \begin{bmatrix} 7000 & 0 \\ 0 & 0.00001 \end{bmatrix}. \tag{48}$$

With the given parameter matrices and weighting matrices, the feedback control input is obtained from the state variables:

$$U = -R^{-1}B^T KX, \tag{49}$$

where K is calculated from the following Riccati equation:

$$-KA - A^T K + KBR^{-1}B^T K - Q = 0. \tag{50}$$

DMT is implemented on each motor to obtain the required yaw moment calculated from Equation (49). It is allocated to front and rear motors according to wheel vertical loads, and then allocated to left and right motors equally but in opposite directions. Combining the vehicle speed PID control input and path following control input, motor torque at each wheel is:

$$\begin{aligned} T_{mfl} &= \frac{l_r r_e (u - M_\gamma / l_t)}{2(l_f + l_r)}, \; T_{mfr} = \frac{l_r r_e (u + M_\gamma / l_t)}{2(l_f + l_r)}, \; T_{mrl} \\ &= \frac{l_f r_e (u - M_\gamma / l_t)}{2(l_f + l_r)}, \; T_{mrr} = \frac{l_f r_e (u + M_\gamma / l_t)}{2(l_f + l_r)}. \end{aligned} \tag{51}$$

The control strategy is also depicted in Figure 10.

6 | VEHICLE PATH FOLLOWING CONTROL SIMULATION RESULTS

To investigate the effectiveness of the path following control strategy and compare two vehicle models under control, a standard double lane change simulation is conducted following the standard of ISO 3888-1:2018 [42]. In the simulation, the lane centreline is set as the reference path. At each turn, an arc with a 2 m radius is used to smooth the desired path. The double lane change is conducted with vehicle speed at 25 km/h and 65 km/h, respectively, to compare two models under moderate and aggressive driving conditions.

6.1 | Path following control with only FWS

In this simulation, the DMT is deactivated and only FWS is used to follow the desired path. The results are shown in Figures 11–14. It could be found path following is successfully finished with only FWS control. In Figure 11a, at each turn, the desired path curvature and direction change, which requires a rapid FWS control input to reduce errors. When FWS input is applied to the detailed model, the tyre transient dynamics are excited which can be seen from the vibrating lateral force in Figure 11c. The vehicle sideslip angle and yaw rate also fluctuate under the vibrating lateral force. Comparatively, the bicycle model doesn't show any transient process where lateral force, sideslip angle and yaw rate all change smoothly. Figure 11g clearly shows the difference between two models where detailed model demonstrates vehicle lateral acceleration fluctuations but bicycle model does not.

The path offsets in bicycle model and detailed model are very close as shown in Figure 12. For instance, the path offset difference between two models is only 1.94% at the first turn, which demonstrates that from the perspective of path following performance evaluation, the bicycle model is suitable for vehicle dynamic control research during mild and moderate driving conditions even though it is not sufficient to represent the transient vibrations.

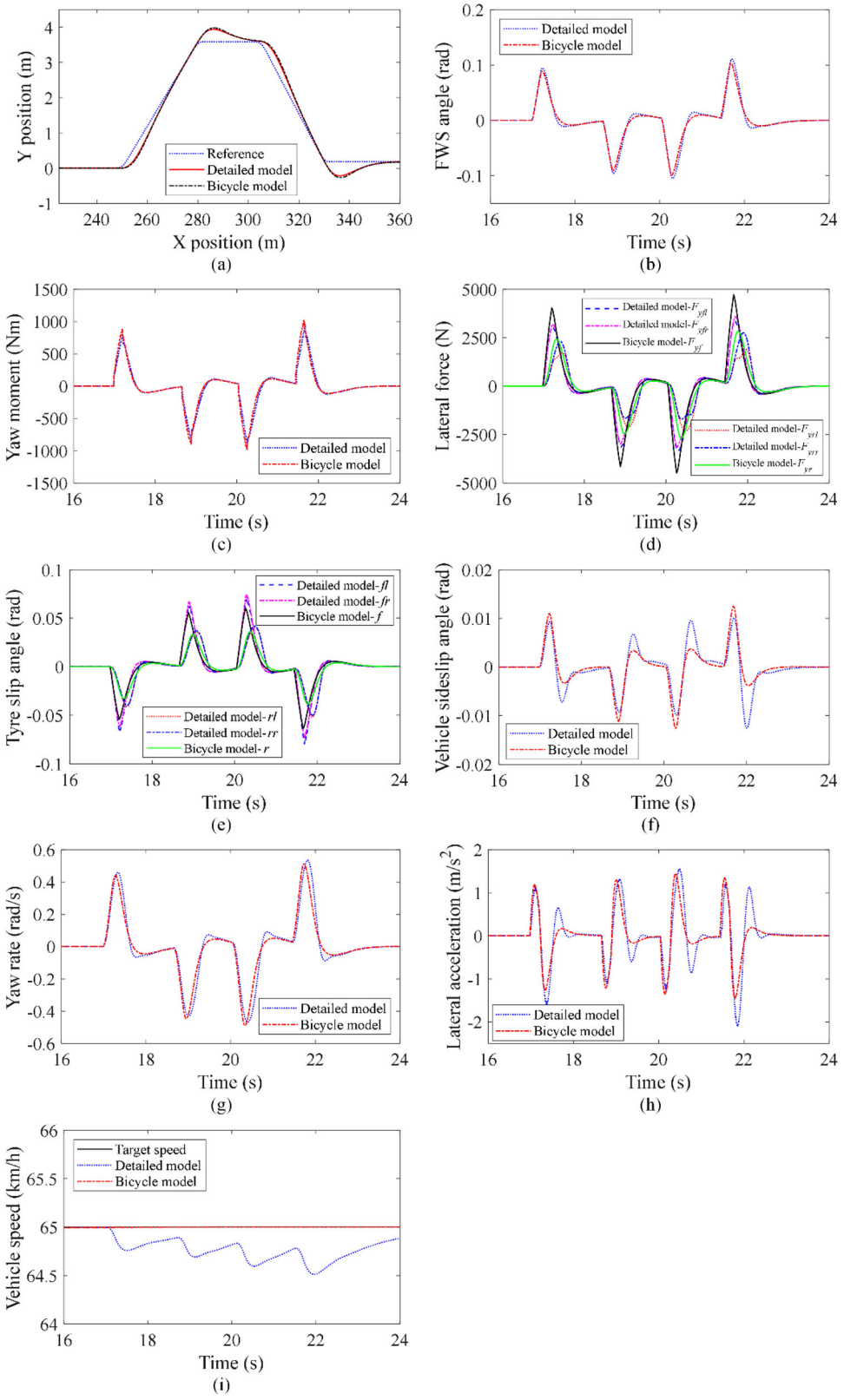

FIGURE 17 Vehicle path following control with combined FWS and MDT at 65 km/h.

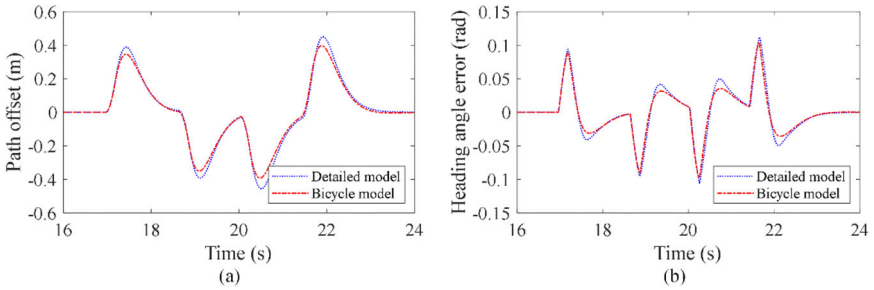

FIGURE 18 Vehicle path following error with combined FWS and MDT at 65 km/h.

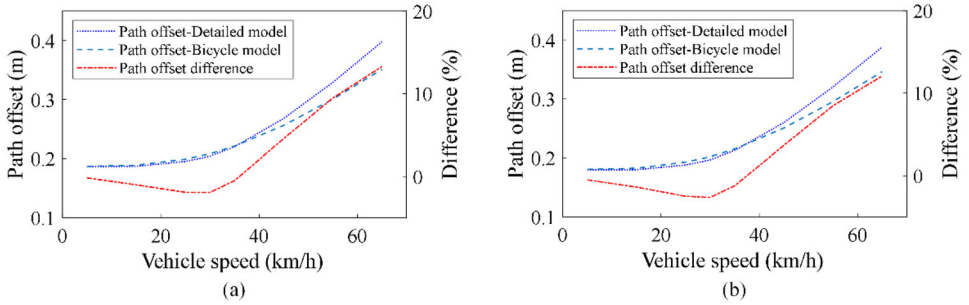

FIGURE 19 Comparison of path offset difference between two models at different vehicle speeds, (a) only FWS control, (b) combined FWS and DMT control.

When vehicle speed is increased to 65 km/h as shown in Figure 13, the path following control is also finished with LQR controller. However, the required lateral force is significantly increased to achieve the desired vehicle movement, as shown in Figure 13c. Moreover, front tyres lateral force is much larger than rear tyres. This indicates that the tyre road friction couldn't be fully used for vehicle dynamic control because when front tyres force is saturated, there is still considerable rear tyres force available. When the same FWS input applies to two models, lateral force in the detailed model increases slower than in the bicycle model due to tyre stiffness and damping. The vehicle sideslip angle and yaw rate in detailed model also show remarkable fluctuations. As shown in Figure 14, at this speed, the detailed model path offset is 13.29 % more than bicycle model, which proves a limit of the bicycle model authenticity to represent vehicle movements.

6.2 | Path following control with combined FWS and DMT

The results of vehicle path following control with combined FWS and DMT at 25 km/h are shown in Figures 15 and 16. It could be found that in addition to FWS input, there is also DMT input which generates yaw moment. Figure 15c shows that in the detailed model, tyre dynamics bring fluctuations to yaw moment while yaw moment is much smoother in the bicycle model. The lateral force also experiences vibrations under FWS and DMT inputs. The vibrating force and torque cause transient process to vehicle movement as shown in vehicle lateral acceleration, sideslip angle and yaw rate. It is worth noticing that although tyre dynamics have significant impact on vehicle transient responses during path following control, which is overlooked in bicycle model, the bicycle model is still useful to research path following errors. This is demonstrated in Figure 16a where the difference in path offset at the first turn is 2.55 % between two models.

Figure 17 shows the results of vehicle double lane change under FWS and DMT control at 65 km/h. It could also be found with high vehicle speed, the required FWS and DMT control inputs are increased. The generated yaw moment and lateral force still fluctuate. As demonstrated in Figure 13c, when only FWS is used for path following control, the rear tyre road friction couldn't be fully used. However, when DMT is applied, lateral force generated on rear tyres is increased. Compared with Figure 13c, rear tyres lateral force is increased while front tyres lateral force is decreased in Figure 17c. Therefore, one of the advantages of combining FWS and DMT control is that lateral tyre force of front and rear tyres could be adjusted to better exploit the tyre road friction. The difference in path offset between two models is 10.77% which is decreased compared with only FWS control, as shown in Figure 18a.

The path offset difference between two models at different vehicle speeds is researched based on the first turn, as shown in Figure 19. It could be found that in only FWS control scenario and combined FWS and DMT control scenario, the path offset both increases with higher vehicle speed. When vehicle speed is lower than 40 km/h, two models have very close path offsets. However, when vehicle speed is higher than 40 km/h, the difference increases rapidly. The fundamental reason is that when vehicle speed is higher, a larger tyre lateral force is required for vehicle movement control. Therefore, the tyre slip angle increases and tyre nonlinearity deviates from the linear tyre characteristics assumption.

7 | CONCLUSION

In this paper, the effect of tyre dynamics on autonomous vehicle path following control is researched by comparing the normally used bicycle model and a detailed vehicle model containing tyre dynamics. In the detailed vehicle model, tyre model is built which reveals the origin of tyre vibration, force hysteresis and nonlinearity. In the open loop test, the same FWS and DMT inputs are applied to two models. The results show that tyre dynamics generate remarkable vehicle transient vibrations and path deviations. Considering the real application of autonomous vehicle path following control, LQR-based feedback control strategy is applied to the vehicle for path following control. It is found that vehicle transient vibrations still exist. The path offset difference between two models is only about 2% with low vehicle speed, which demonstrates that the bicycle vehicle model is suitable for autonomous vehicle path following performance evaluation during moderate driving conditions. When vehicle runs at high speed and requires high tyre force, tyre presents more nonlinearity which makes the path offset difference between two models over 10%. In these scenarios, the bicycle model authenticity is limited to represent vehicle dynamics. What is more, path following control could be realized by only FWS control or combined FWS and DMT control. The results show that combined FWS and DMT control achieves smaller path following errors than only FWS control. Combined FWS and DMT control could also adjust the front tyres and rear tyres' lateral force to maximally exploit tyre road frictions. In future research, advanced vehicle dynamic control strategies should be designed to tackle the complicated tyre dynamics so that they can achieve the ideal control effects when implemented in real vehicles. What's more, the real time vehicle parameters are essential for control strategies, which requires parameter estimation algorithms to be designed to obtain the unmeasurable parameters and eliminate measurement noise. Finally, experiments are necessary to vitrify the effectiveness and practicality of the control strategies and hardware control systems.

ACKNOWLEDGEMENTS

This work is funded by Natural Science Foundation of Hebei Province (E2021203085), Yanshan University (2021LGQN008) and Hebei Province Department of Education (C20220330).

CONFLICT OF INTEREST STATEMENT

The authors declare that there is no conflict of interest

DATA AVAILABILITY STATEMENT

All the parameters and results are provided in the paper.

ORCID

Shilei Zhou https://orcid.org/0000-0001-5070-141X

REFERENCES

1. Hu, C., Wang, Z., Qin, Y., Huang, Y., Wang, J., Wang, R.: Lane Keeping Control of Autonomous Vehicles With Prescribed Performance Considering the Rollover Prevention and Input Saturation. IEEE Trans. Intell. Transp. Syst. 21(7), 3091–3103 (2020)
2. Murata, S.: Innovation by in-wheel-motor drive unit. Veh. Syst. Dyn. 50(6), 807–830 (2012)
3. Ataei, M., Khajepour, A., Jeon, S.: Model Predictive Control for integrated lateral stability, traction/braking control, and rollover prevention of electric vehicles. Veh. Syst. Dyn. 58, 49–73 (2019)
4. Hu, C., Wang, R., Yan, F., Karimi, H.R.: Robust Composite Nonlinear Feedback Path-Following Control for Independently Actuated Autonomous Vehicles With Differential Steering. IEEE Trans. Transp. Electrif. 2(3), 312–321 (2016)
5. Shim, T., Adireddy, G., Yuan, H.: Autonomous vehicle collision avoidance system using path planning and model-predictive-control-based active front steering and wheel torque control. Proc. Inst. Mech. Eng. Part D: J. Automob. Eng. 226(6), 767–778 (2012)
6. Zhang, L., Li, L., Qi, B.: Rollover prevention control for a four in-wheel motors drive electric vehicle on an uneven road. Sci. China Technolog. Sci. 61(6), 934–948 (2017)
7. Wang, J., Wang, Q., Jin, L., Song, C.: Independent wheel torque control of 4WD electric vehicle for differential drive assisted steering. Mechatronics 21(1), 63–76 (2011)
8. Kirli, A., Chen, Y., Okwudire, C.E., Ulsoy, A.G.: Torque-Vectoring-Based Backup Steering Strategy for Steer-by-Wire Autonomous Vehicles With Vehicle Stability Control. IEEE Trans. Veh. Technol. 68(8), 7319–7328 (2019)
9. Zhu, J., Wang, Z., Zhang, L., Dorrell, D.G.: Braking/steering coordination control for in-wheel motor drive electric vehicles based on nonlinear model predictive control. Mech. Mach. Theory 142, 103586 (2019)
10. Wang, Y., Cheng, Q., Gao, L., Zhang, W.: The Control Strategy Research of 4WID Vehicles Steering-by-Wire System. J. Phys. Conf. Ser. 1650(2), 022041 (2020)
11. Mousavinejad, E., Han, Q.-L., Yang, F., Zhu, Y., Vlacic, L.: Integrated control of ground vehicles dynamics via advanced terminal sliding mode control. Veh. Syst. Dyn. 55(2), 268–294 (2016)
12. Li, X., Xu, N., Guo, K., Huang, Y.: An adaptive SMC controller for EVs with four IWMs handling and stability enhancement based on a stability index. Veh. Syst. Dyn. 59, 1509–1532 (2020)
13. Shuai, Z., Zhang, H., Wang, J., Li, J., Ouyang, M.: Combined AFS and DYC Control of Four-Wheel-Independent-Drive Electric Vehicles over CAN Network with Time-Varying Delays. IEEE Trans. Veh. Technol. 63(2), 591–602 (2014)
14. Xu, S., Peng, H., Song, Z., Chen, K., Tang, Y.: Design and test of speed tracking control for the self-driving lincoln MKZ platform. IEEE Trans. Intell. Veh. 5(2), 324–334 (2020)
15. Wang, Y., Ding, H., Yuan, J., Chen, H.: Output-feedback triple-step coordinated control for path following of autonomous ground vehicles. Mech. Syst. Sig. Process. 116, 146–159 (2019)
16. Wang, R., Hu, C., Yan, F., Chadli, M.: Composite nonlinear feedback control for path following of four-wheel independently actuated autonomous ground vehicles. IEEE Trans. Intell. Transp. Syst. 17(7), 2063–2074 (2016)
17. Mohammadzadeh, A., Taghavifar, H.: A novel adaptive control approach for path tracking control of autonomous vehicles subject to uncertain dynamics. Proc. Inst. Mech. Eng. Part D: J. Automob. Eng. 234(8), 2115–2126 (2020)
18. Cao, H., et al.: An optimal hierarchical framework of the trajectory following by convex optimisation for highly automated driving vehicles. Veh. Syst. Dyn. 57(9), 1287–1317 (2018)
19. Schmeitz, A.J.C., Besselink, I.J.M., Jansen, S.T.H.: Tno Mf-Swift. Veh. Syst. Dyn. 45(sup1), 121–137 (2007)
20. Maurice, J.P., Zegelaar, P.W.A., Pacejka, H.B.: The influence of belt dynamics on cornering and braking properties of tyres. Veh. Syst. Dyn. 29(sup1), 299–311 (1998)
21. Zegelaar, P.W.A., Pacejka, H.B.: Dynamic tyre responses to brake torque variations. Veh. Syst. Dyn. 27(sup001), 65–79 (1997)
22. Maurice, J.P., Pacejka, H.B.: Relaxation length behaviour of tyres. Veh. Syst. Dyn. 27(sup001), 339–342 (1997)

23. Li, Y., Min, X., Tong, S.: Observer-based fuzzy adaptive inverse optimal output feedback control for uncertain nonlinear systems. IEEE Trans. Fuzzy Syst. 29(6), 1484–1495 (2021)
24. Li, Y., Sun, K., Tong, S.: Observer-based adaptive fuzzy fault-tolerant optimal control for SISO nonlinear systems. IEEE Trans Cybern 49(2), 649–661 (2019)
25. Eising, C., Pereira, L.F., Horgan, J., Selvaraju, A., McDonald, J., Moran, P.: 2.5D vehicle odometry estimation. IET Intel. Transport Syst. 16(3), 292–308 (2021)
26. Brunker, A., Wohlgemuth, T., Frey, M., Gauterin, F.: Odometry 2.0: A slip-adaptive EIF-based four-wheel-odometry model for parking. IEEE Trans. Intell. Veh. 4(1), 114–126 (2019)
27. Liu, W., Xiong, L., Xia, X., Lu, Y., Gao, L., Song, S.: Vision-aided intelligent vehicle sideslip angle estimation based on a dynamic model. IET Intel. Transport Syst. 14(10), 1183–1189 (2020)
28. Brown, M., Gerdes, J.C.: Coordinating tire forces to avoid obstacles using nonlinear model predictive control. IEEE Trans. Intell. Veh. 5(1), 21–31 (2020)
29. Yutao, L., Di, T.: Study on the Dynamics of the In-Wheel Motor System. IEEE Trans. Veh. Technol. 61(8), 3510–3518 (2012)
30. Mi, T., Stepan, G., Takacs, D., Chen, N.: Shimmy model for electric vehicle with independent suspensions. Proc. Inst. Mech. Eng., Part D: J. Automob. Eng. 232(3), 330–340 (2017)
31. Li, S.E., Chen, H., Li, R., Liu, Z., Wang, Z., Xin, Z.: Predictive lateral control to stabilise highly automated vehicles at tire-road friction limits. Veh. Syst. Dyn. 58(5), 768–786 (2020)
32. Zhang, J., et al.: Adaptive sliding mode-based lateral stability control of steer-by-wire vehicles with experimental validations. IEEE Trans. Veh. Technol. 69(9), 9589–9600 (2020)
33. Wang, J., Zhang, G., Wang, R., Schnelle, S.C., Wang, J.: A gain-scheduling driver assistance trajectory-following algorithm considering different driver steering characteristics. IEEE Trans. Intell. Transp. Syst. 18(5), 1097–1108 (2017)
34. Jing, H., Wang, R., Wang, J., Chen, N.: Robust H∞ dynamic output-feedback control for four-wheel independently actuated electric ground vehicles through integrated AFS/DYC. J. Franklin Inst. 355(18), 9321–9350 (2018)
35. Ma, Z., Ji, X., Zhang, Y., Yang, J.: State estimation in roll dynamics for commercial vehicles. Veh. Syst. Dyn. 55(3), 313–337 (2016)
36. Termous, H., Shraim, H., Talj, R., Francis, C., Charara, A.: Coordinated control strategies for active steering, differential braking and active suspension for vehicle stability, handling and safety improvement. Veh. Syst. Dyn. 57(10), 1494–1529 (2018)
37. Choi, M.W., Park, J.S., Lee, B.S., Lee, M.H.: The performance of independent wheels steering vehicle (4WS) applied Ackerman geometry. In: 2008 International Conference on Control, Automation and Systems, pp. 197–202. IEEE, Piscataway (2008)
38. Pacejka, H.: Tire and Vehicle Dynamics. Elsevier, Amsterdam (2005)
39. Laurense, V.A., Gerdes, J.C.: Long-horizon vehicle motion planning and control through serially cascaded model complexity. IEEE Trans. Control Syst. Technol. 30(1), 166–179 (2021)
40. Xu, S., Peng, H., Tang, Y.: Preview path tracking control with delay compensation for autonomous vehicles. IEEE Trans. Intell. Transp. Syst. 22(5), 2979–2989 (2020)
41. Xu, S., Peng, H.: Design, Analysis, Experiments of Preview Path Tracking Control for Autonomous Vehicles. IEEE Trans. Intell. Transp. Syst. 21(1), 48–58 (2020)
42. International Organization for Standardization: ISO 3888-1:2018 Passenger cars — Test track for a severe lane-change manoeuvre — Part 1: Double lane-change (2018)

How to cite this article: Zhou, S., Tian, Y., Walker, P., Zhang, N.: Impact of the tyre dynamics on autonomous vehicle path following control with front wheel steering and differential motor torque. IET Intell. Transp. Syst. 17, 1629–1648 (2023). https://doi.org/10.1049/itr2.12356